

## Imaging magnetic vortex configurations in ferromagnetic nanotubes

M. Wyss,<sup>1</sup> A. Mehlin,<sup>1</sup> B. Gross,<sup>1</sup> A. Buchter,<sup>1</sup> A. Farhan,<sup>2,3</sup> M. Buzzi,<sup>4</sup> A. Kleibert,<sup>4</sup> G. Tütüncüoğlu,<sup>5</sup> F. Heimbach,<sup>6</sup>  
A. Fontcuberta i Morral,<sup>5</sup> D. Grundler,<sup>7</sup> and M. Poggio<sup>1,\*</sup>

<sup>1</sup>Department of Physics, University of Basel, 4056 Basel, Switzerland

<sup>2</sup>Laboratory for Micro- and Nanotechnology, Paul Scherrer Institute, 5232 Villigen, Switzerland

<sup>3</sup>Laboratory for Mesoscopic Systems, Department of Materials, ETH Zürich, 8093 Zürich, Switzerland

<sup>4</sup>Swiss Light Source, Paul Scherrer Institute, 5232 Villigen, Switzerland

<sup>5</sup>Laboratory of Semiconductor Materials, Institute of Materials (IMX), School of Engineering, École Polytechnique Fédérale de Lausanne (EPFL), 1015 Lausanne, Switzerland

<sup>6</sup>Lehrstuhl für Physik funktionaler Schichtsysteme, Physik Department E10, Technische Universität München, 85747 Garching, Germany

<sup>7</sup>Laboratory of Nanoscale Magnetic Materials and Magnonics, Institute of Materials (IMX), School of Engineering, École Polytechnique Fédérale de Lausanne (EPFL), 1015 Lausanne, Switzerland

(Received 21 February 2017; published 17 July 2017)

We image the remnant magnetization configurations of CoFeB and permalloy nanotubes (NTs) using x-ray magnetic circular dichroism photoemission electron microscopy. The images provide direct evidence for flux-closure configurations, including a global vortex state, in which magnetization points circumferentially around the NT axis. Furthermore, micromagnetic simulations predict and measurements confirm that vortex states can be programmed as the equilibrium remnant magnetization configurations by reducing the ratio of the NT's length and diameter.

DOI: [10.1103/PhysRevB.96.024423](https://doi.org/10.1103/PhysRevB.96.024423)

### I. INTRODUCTION

The study of magnetic nanostructures is motivated by their potential as elements in dense magnetic memories, logical devices [1], magnetic sensors [2], and as probes in high-resolution imaging applications [3–5]. For these reasons, a number of nanometer-scale geometries have been investigated both theoretically and experimentally, including magnetic dots, rings, wires, and tubes. Of particular interest are nanomagnets with stable flux-closure magnetization configurations and both fast and reproducible reversal processes. In the context of magnetic memory, speed and reliability are determined by the latter, while ultimate density can be enhanced by the former. Although flux-closure configurations require dimensions significantly larger than the dipolar exchange length, they favor high density, because they produce minimal stray fields, thereby minimizing interactions between nearby memory elements [6].

Ferromagnetic nanotubes (NTs) are a particularly promising morphology, given their lack of a magnetic core. At equilibrium, the hollow magnetic geometry is expected to stabilize vortex-like flux-closure configurations with magnetization pointing along the NT circumference. Although vortex ends states have been observed in ferromagnetic nanowires (NWs) [7], the exchange energy penalty for the magnetic singularity along the vortex axis tends to favor non-flux-closure states. In a NT, the lack of this axial Bloch point structure [8] is also expected to allow for fast magnetization reversal that begins with vortices nucleating at its ends and propagating along its length [9–11]. Due to their tubular geometry, NTs may reveal curvature-induced effects [12,13], such as asymmetric spin-wave dispersion [14] or Cherenkov-

type emission of magnons by certain types of domain walls [15]. Theoretical studies of magnetization configurations in ferromagnetic NTs have predicted an equilibrium flux-closure configuration, the so-called global vortex state, as well as other configurations, including a uniform axial state and a mixed state [11]. In a global vortex state, the entire NT's magnetization is circumferentially aligned, while the mixed state combines vortex-like ends, minimizing magnetostatic energy, and an axially aligned center, minimizing exchange energy. Calculations suggest that for short NTs, opposing vortex states, in which two vortices with opposing circulation are separated by a Néel domain wall, may also be stable [16]. The dependence of the NT's equilibrium magnetization configuration on geometry, as well as details such as the relative sense of circulation of the end-vortices, have been considered both analytically and numerically [16–18]. In particular, it has been predicted that the global vortex state can be programmed as the stable remnant configuration by a small NT length-to-diameter ratio.

Experimental evidence for vortex configurations in NTs has so far been limited to magnetic force microscopy images of single NTs reported by Li *et al.* [19]. There, the authors interpret a nearly vanishing MFM contrast and a small remnant magnetization as an indication of a global vortex state. Magnetotransport [20] and dynamic cantilever magnetometry (DCM) [21] of Ni NTs suggest the presence of vortex configurations; however, the considerable roughness of these NTs likely makes them different enough from idealized ferromagnetic NTs to affect their equilibrium configurations. Magnetization configurations in rolled-up ferromagnetic membranes between 2 and 16  $\mu\text{m}$  in diameter have been imaged using magneto-optical Kerr effect [22], x-ray transmission microscopy [22], x-ray magnetic dichroism photoemission electron microscopy (XMCD-PEEM) [23], and magnetic soft x-ray tomography [24]. In these studies, the authors report azimuthal domain

\*martino.poggio@unibas.ch

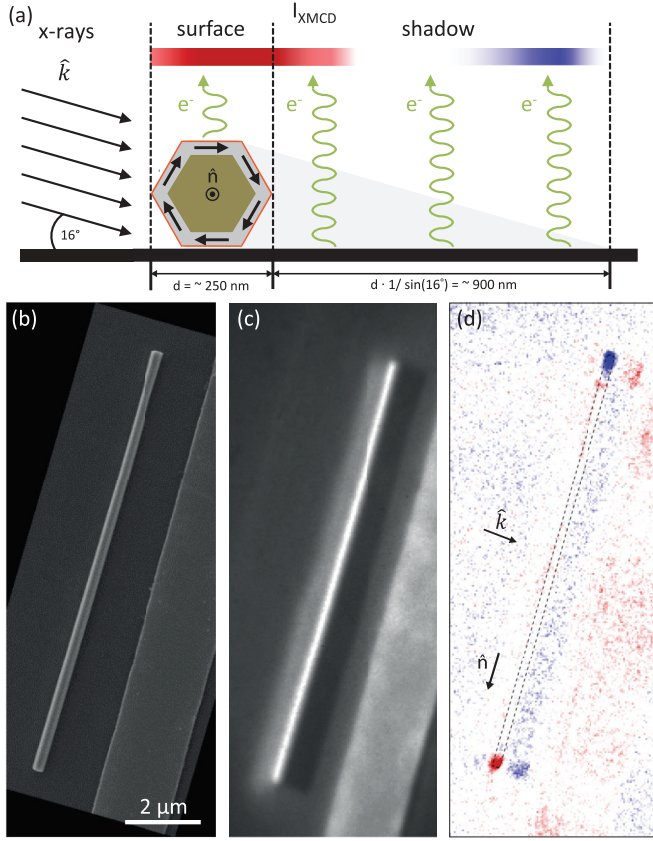


FIG. 1. (a) Schematic drawing of a NT cross-section with incident x rays, photoexcited electrons, and expected XMCD-PEEM contrast for the depicted vortex configuration. The brown central region depicts the nonmagnetic GaAs template material, the gray region the magnetic NT, and the red region the native oxide. (b) SEM of an 11.3- $\mu\text{m}$ -long CoFeB NT with a Au alignment marker visible on the right of the image. (c) PEEM image with grayscale contrast corresponding to  $I_{\text{PEEM}}$  and (d) XMCD-PEEM image with red (blue) contrast representing positive (negative)  $I_{\text{XMCD}}$ . The dashed line shows the position of the NT.

patterns that are commensurable throughout the windings and attribute the effect to magnetostatic [23,24] or exchange [22] coupling between windings.

Here we use XMCD-PEEM [7,8,25] to image magnetic configurations in individual magnetic NTs, which are an order of magnitude smaller. These NTs are prepared as continuous magnetic shells around nanotemplates, allowing for both magnetostatic and exchange coupling. We find remnant global vortex states and show that length-to-diameter ratio can be used to program the occurrence of different remnant states, including mixed, opposing vortex, and global vortex states.

## II. SAMPLES

We study CoFeB and  $\text{Ni}_{80}\text{Fe}_{20}$  (permalloy) NTs consisting of a non-magnetic GaAs core surrounded by a 30-nm-thick magnetic shell with a hexagonal cross-section, as shown in Fig. 1(a). Their diameter  $d$ , which we define as the diameter of the circle circumscribing the hexagonal cross-section, is between 200 and 300 nm and their length  $l$  between 0.5 and

12  $\mu\text{m}$ . We obtain specific lengths and well-defined ends by cutting individual NTs into segments using a focused ion beam (FIB). After cutting, we use an optical microscope equipped with precision micromanipulators to pick up the NT segments and align them horizontally onto a Si substrate. Scanning electron micrographs (SEMs) of the 19 CoFeB and 25 permalloy (Py) NTs studied [26] reveal continuous surfaces, which are free of detectable defects and whose roughness is less than 5 nm. The fabrication process and choice of materials avoids magneto-crystalline anisotropy [27–29], although recent magnetotransport experiments suggest that a growth-induced magnetic anisotropy may be present in the CoFeB NTs [30]. DCM measurements of NTs from the same growth wafers as used here provide  $\mu_0 M_S = 1.3 \pm 0.1$  T and  $0.8 \pm 0.1$  T for the CoFeB [31] and Py [32] NTs, respectively, where  $\mu_0$  is the permeability of free space. The magnetic shell material is covered by a few-nanometer-thick native oxide, which affects the NT magnetization only at cryogenic temperatures through antiferromagnetic exchange coupling. In Py NTs, Buchter *et al.* observed such coupling below a blocking temperature of 18 K [32].

## III. XMCD-PEEM

XMCD-PEEM measurements are performed at the Surface/Interface: Microscopy (SIM) beamline of the Swiss Light Source (SLS) at the Paul Scherrer Institut (PSI) [33]. Experiments are carried out at room temperature and in remanence. Circularly polarized x rays tuned to the  $L_3$ -edge of Fe propagating along  $\hat{k}$  impinge on the Si sample substrate with an incident angle of  $16^\circ$ , as shown schematically in Fig. 1(a). The apparatus allows the rotation of the sample about the substrate normal with respect to  $\hat{k}$ , which is fixed. XMCD-PEEM images are obtained by taking the difference of PEEM images taken with x rays of opposite helicity  $\sigma^+$  and  $\sigma^-$  normalized to their sum:  $I_{\text{XMCD}} = (I_{\sigma^+} - I_{\sigma^-}) / (I_{\sigma^+} + I_{\sigma^-})$ , where  $I_{\sigma^\pm}$  represents the emission intensity of photoelectrons, which is proportional to the local absorption cross-section of  $\sigma^\pm$  polarized x-ray illumination. The spatial resolution of the images is about 100 nm.

A SEM of a representative 11.3- $\mu\text{m}$ -long CoFeB nanotube is shown in Fig. 1(b). A PEEM image of the same NT in Fig. 1(c) shows  $I_{\text{PEEM}} = (I_{\sigma^+} + I_{\sigma^-})/2$  with the NT long axis  $\hat{n}$  aligned perpendicular to the x-ray beam appears. Due to the resonant excitation of the Fe  $L_3$ -edge, PEEM contrast from the NT surface appears as the brightest feature. The dark stripe on the right of the NT is a shadow effect resulting from the grazing incidence of the incident x rays and their partial attenuation by the NT. A bright region to the left of the NT appears due to x rays reflected by the smooth surface of the NT. A dotted outline shows the position of the NT in the corresponding XMCD-PEEM image in Fig. 1(d), as determined by overlaying SEM, PEEM, and XMCD-PEEM images of the same NT (see Appendix B).  $I_{\text{XMCD}}$  within the outline stems from a region on top of the NT within 3 to 5 nm of the surface and is proportional to the projection of its local magnetization along  $\hat{k}$ .  $I_{\text{XMCD}}$  in the shadow on the right of the outline—on the nonmagnetic Si surface—depends on the imbalance in the intensity of  $\sigma^\pm$  x rays transmitted through the magnetic material, rather than any surface magnetization [8]. The contrast in the shadow region is

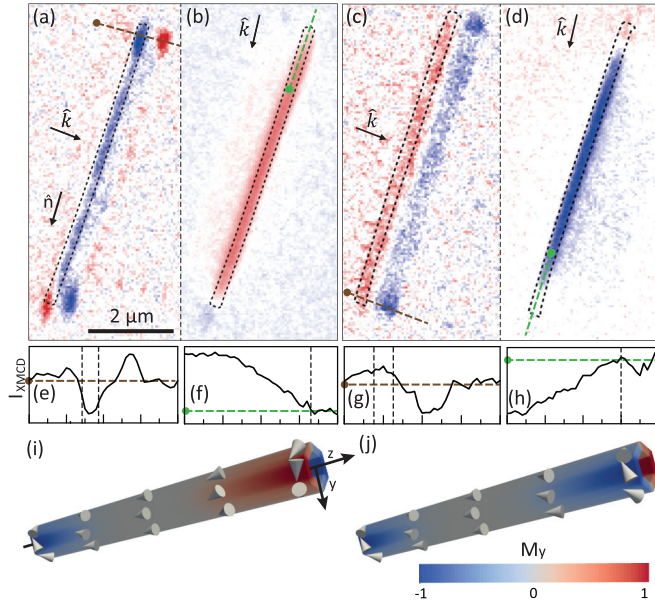


FIG. 2. XMCD-PEEM images of a 6.9- $\mu\text{m}$ -long Py NT with (a)  $\hat{k} \perp \hat{n}$  and (b)  $\hat{k} \parallel \hat{n}$  and of a 7.2- $\mu\text{m}$ -long CoFeB NT with (c)  $\hat{k} \perp \hat{n}$  and (d)  $\hat{k} \parallel \hat{n}$ . Dashed outlines indicate the positions of the NTs. Panels (e–h) represent 2- $\mu\text{m}$ -long  $I_{\text{XMCD}}$  linecuts along the corresponding colored dashed lines in (a–d). In the linecuts, the background intensity is indicated by the level of the horizontal dashed lines and vertical dashed lines delineate the boundaries of the NT. Panels (i) and (j) show simulated remnant magnetic states for a NT with  $l = 2.1 \mu\text{m}$  and  $d = 245 \text{ nm}$ . Both configurations are mixed states with an axial central domain and vortex ends of either (i) opposing circulation—consistent with (a) and (b)—or (j) matching circulation—consistent with (c) and (d). The color scale corresponds to normalized magnetization along  $\hat{y}$ . Arrowheads indicate the local magnetization direction.

therefore sensitive to the average magnetization of the volume traversed by the x rays, with opposite sign compared to surface contrast (see Appendix B). The lack of surface and shadow  $I_{\text{XMCD}}$  contrast corresponding to the central part of the NT in Fig. 1(d) indicates negligible magnetization oriented parallel to  $\hat{k}$  (perpendicular to  $\hat{n}$ ). On the other hand, at the NT ends, strong surface and shadow contrast indicates magnetization oriented parallel to  $\hat{k}$  (perpendicular to  $\hat{n}$ ).

XMCD-PEEM images with  $\hat{k} \perp \hat{n}$  (perpendicular XMCD-PEEM contrast) are shown in Figs. 2(a) and 2(c) for Py and CoFeB NTs with lengths of 6.9 and 7.2  $\mu\text{m}$ , respectively. Contrast similar to that of Fig. 1(d) shows magnetization oriented perpendicular to  $\hat{n}$  near the ends of the NTs. Further information is gleaned by rotating the sample stage relative to  $\hat{k}$  and performing the same measurements with  $\hat{k} \parallel \hat{n}$  (parallel XMCD-PEEM contrast), as shown in Figs. 2(b) and 2(d). In this case, strong surface contrast in the central part of the NT indicates magnetization parallel to  $\hat{n}$ . Decreased contrast at the NT ends confirms a magnetization oriented perpendicular to  $\hat{n}$ , as suggested by the measurements with  $\hat{k} \perp \hat{n}$ . In Figs. 2(a) and 2(c), residual surface and shadow contrast corresponding to the central parts of the NTs may be due to a slightly tilted axial magnetization or an imperfect perpendicular alignment of the x rays with respect to the NTs. The latter explanation may also

account for the tilt in the opposing surface and shadow contrast at the end of the NT with respect to  $\hat{k}$  indicated in Fig. 2(a). Also, despite the strong shadow contrast from the ends in Fig. 2(c), the corresponding surface contrast is weak. This lack of contrast is likely due to oxidation of the NT surface. Given the limited probing depth related to the surface contrast and the fact that the shadow contrast originates from the magnetization within the NT, in such cases, we rely on  $I_{\text{XMCD}}$  in the shadow to determine the NT's magnetic configuration.

Specific magnetization configurations in a magnetic nanostructure produce characteristic XMCD-PEEM signatures for a given orientation of  $\hat{k}$ . Following the procedure described by Jamet *et al.*, which takes into account the progressive absorption of the x-ray beam through the sample cross-section [7], a vortex configuration in our NTs should result in perpendicular XMCD-PEEM contrast of the form shown in Fig. 1(a). This contrast is characterized by both strong surface and shadow contrast (due to the component of the magnetization aligned parallel to  $\hat{k}$ ) and a change of sign in the x-ray shadow. Figures 2(e) and 2(g) show linecuts through the perpendicular XMCD-PEEM image at the NT ends consistent with this expectation. However, since the NTs lie directly on the substrate and are not suspended as in Jamet *et al.*, part of the shadow is occluded. As a result, surface and shadow contrast partially merge, making it difficult to distinguish the sign reversal in the shadow. As a result, although the presence of remnant vortex domains is strongly supported by simulations discussed in Sec. IV and shown in Figs. 2(i) and 2(j), their unambiguous identification is not possible on the basis of these images alone. Figures 2(f) and 2(h) show linecuts of parallel XMCD-PEEM images through the same region along  $\hat{n}$ . The reduction in the surface contrast near the end of the NT relative to the central region is also consistent with decreasing on-axis magnetization due to a vortex end state. The complementarity of vanishing and strong contrast in the central part of the NT in the perpendicular and parallel XMCD-PEEM images, respectively, provides strong evidence for an axially aligned central region. Taken together, these images point to a mixed state configuration, where magnetic moments in the central part of the NT align along its long axis and curl into vortices at the ends. The relative sign of the perpendicular XMCD-PEEM contrast at the ends of the NTs shown in Figs. 2(a) and 2(c) indicates that they are in mixed states with end vortices of opposing and matching circulation, respectively.

For NTs of either material longer than 2  $\mu\text{m}$ , we find remnant mixed states with vortices of both opposing and matching circulation, as in Fig. 2 [26]. For NTs shorter than 2  $\mu\text{m}$ , different magnetization configurations emerge. Figure 3(a) shows both perpendicular and parallel XMCD-PEEM images of a 1.30- $\mu\text{m}$ -long Py nanotube. In the perpendicular image, nearly all magnetic moments point perpendicular to  $\hat{n}$  and show the signature of a global vortex state with a single sense of circulation. In the parallel image, a small area of axial moments is visible in the surface contrast, indicating either a slightly tilted vortex configuration or imperfections at the surface of the magnetic shell. Figure 3(b) shows XMCD-PEEM contrast from a 0.73- $\mu\text{m}$ -long Py NT, in which the magnetization points mostly perpendicular to the NT axis. The remnant magnetization configuration, however, does not display a



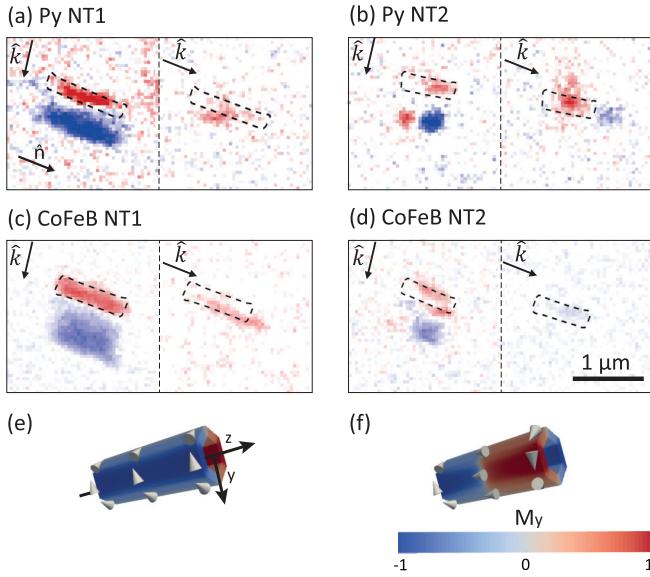


FIG. 3. XMCD-PEEM images with  $\hat{k} \perp \hat{n}$  and  $\hat{k} \parallel \hat{n}$  of short NTs. (a) 1.3- $\mu\text{m}$ -long Py NT found in a global vortex state. (b) 0.73- $\mu\text{m}$ -long Py NT in an opposing vortex state. (c) 1.06- $\mu\text{m}$ -long CoFeB NT in a global vortex state. (d) 0.83- $\mu\text{m}$ -long CoFeB NT in an opposing vortex state. Simulated equilibrium states of ferromagnetic NTs ( $l = 610 \text{ nm}$ ,  $d = 245 \text{ nm}$ ) in (e) a global vortex state and in (f) an opposing vortex state. The color-scale corresponds to the normalized magnetization along  $\hat{y}$ . Arrowheads indicate the local magnetization direction.

vortex with a single circulation sense, but rather two vortices of opposing circulations separated by an axial Néel domain wall. This central wall produces vanishing shadow contrast (white) in the perpendicular image, while showing strong positive (red) surface and negative (blue) shadow contrast in the parallel image, as expected for magnetization aligned along  $\hat{n}$ . We therefore conclude that this NT is in an opposing vortex state. Results for CoFeB NTs of similar sizes are shown in Figs. 3(c) and 3(d). Figure 3(c) shows contrast from a 1.06- $\mu\text{m}$ -long NT in a remnant global vortex state, whereas Fig. 3(d) shows a 0.83- $\mu\text{m}$ -long NT in a remnant opposing vortex state.

#### IV. COMPARISON TO NUMERICAL SIMULATIONS

To corroborate the XMCD-PEEM measurements, we carry out numerical simulations of NT magnetization using the software package *Mumax3* [34]. This package employs the Landau-Lifshitz micromagnetic formalism using a finite-difference discretization. We then compare the numerically expected equilibrium configurations and the experimentally observed remnant configurations as a function of the diameter  $d$  and length  $l$ . Experimental results are extracted from perpendicular and parallel XMCD-PEEM images of each measured NT [26]. Simulations are consistent with our XMCD-PEEM measurements in that long NTs are calculated to have remnant mixed state configurations, as depicted in Figs. 2(i) and 2(j), and short NTs remnant global vortex or opposing vortex states, as depicted in Figs. 3(e) and 3(f). The simulations also reproduce subtleties of the magnetization configuration in the NTs, including the length of the vortex ends and its

dependence on  $d$  [26]. The average length of the vortices along  $\hat{n}$  is measured to be  $320 \pm 50 \text{ nm}$  for CoFeB NTs and  $360 \pm 50 \text{ nm}$  for Py NTs.

Despite the agreement, the relative circulation sense of the end vortices predicted by the simulations does not exactly match our observations. For long NTs in remnant mixed state configurations, the energy difference between a configuration with matching or opposing circulation vortices is calculated to be small compared to the precision of the simulation; therefore, each is predicted to be equally likely. In the real NTs, although the distribution is equal across all NTs, it is unequal for a single material: three opposing and eight matching mixed states appear in CoFeB NTs, while nine opposing and four matching appear in Py NTs. As the length-to-diameter ratio is reduced, simulations indicate that the relative circulation of the end vortices leads to energy differences larger than the thermal energy. As the central region of axial magnetization disappears, matching circulation is eventually favored, resulting in a stable global vortex state. For NTs of both CoFeB and Py short enough to favor matching circulation and therefore a global vortex configuration ( $l \lesssim 2.2 \mu\text{m}$  for CoFeB and  $l \lesssim 1.6 \mu\text{m}$  for Py), we observe seven global and two opposing vortex states in CoFeB NTs and six global, two opposing vortex, and three states that switch configuration upon a second measurement in Py NTs. Although the overall trend confirms the numerical predictions, the discrepancies suggest that imperfections may still be decisive in energetically favoring one configuration over another. Simulations show that in equilibrium the relative circulation sense is sensitive to variations in NT thickness as well as geometrical imperfections, such as slanted rather than flat ends introduced by the FIB cutting process. Given that such imperfections are known to be present, we assume that they play a role in determining the relative circulation of the end vortices.

Note that—for perfect NTs—our simulations show no combination of length and diameter, for which opposing circulation is energetically favored over matching circulation. However, we find that insufficient discretization of the numerical cells can lead to this erroneous result (see Appendix C). It is likely that earlier numerical simulations [35,36], showing the mixed state with end vortices of opposing circulation as the low-field equilibrium configuration, are affected by this artifact and are therefore incorrect.

If we consider NTs measured to have vortices with equal circulation sense, we find that the NT length-to-diameter ratio dictates whether the remnant state is a global vortex state, consistent with the simulations. In Figs. 4(a) and 4(b), NTs measured to be in either a mixed or global vortex state are plotted as a function of  $l$  and  $d$  together with the numerical expectation. We distinguish between a global vortex state and a mixed state with an axially aligned central domain and vortices with equal circulation sense. The presence of the central domain can be quantified by an order parameter  $M_n/|\mathbf{M}|$  corresponding to the relative amount of magnetization that is axially aligned. By plotting this order parameter for numerical simulations of NTs with different lengths and diameters, a clear boundary between the mixed state and global vortex state emerges, as shown in Figs. 4(a) and 4(b). The same classification is carried out on the measurements,

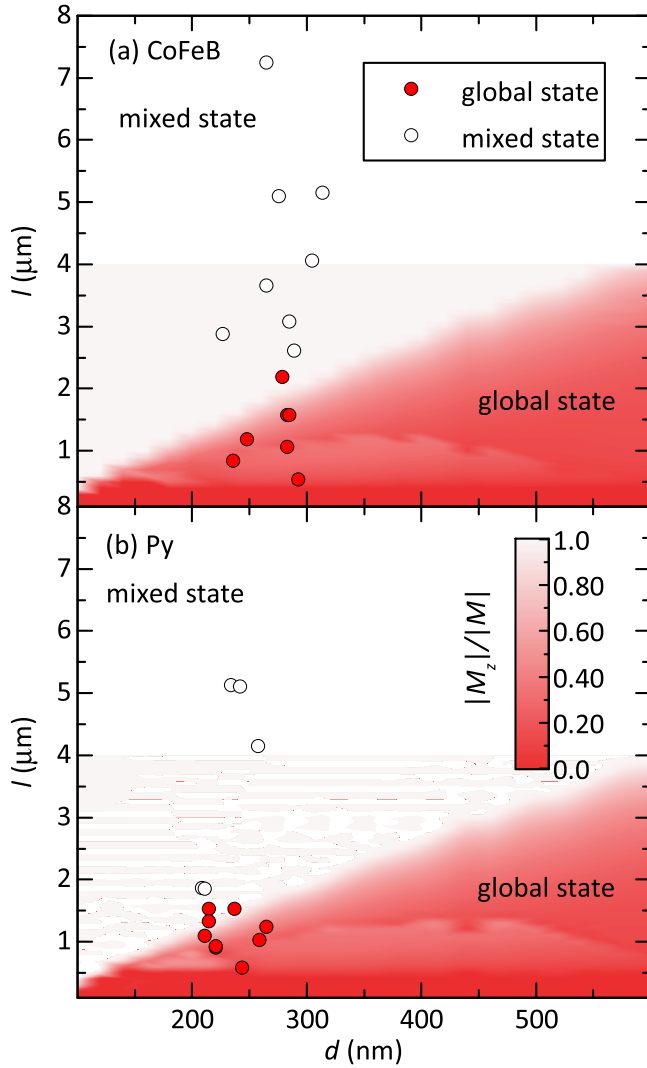


FIG. 4. Phase diagrams for (a) CoFeB and (b) Py NTs as a function of  $l$  and  $d$  considering only magnetization configurations with equal circulation sense. The numerically calculated order parameter  $M_n/|M|$  is plotted in the color scale and defines the boundary between the mixed and global vortex state. Red (white) points show measurements of real NTs in global vortex (mixed) states as measured by XMCD-PEEM [26].

with the global vortex state determined by the absence of a well-resolved axial domain in the XMCD-PEEM images. The measured dependence of magnetic configuration on geometry not only agrees closely with the numerical simulations, but is also qualitatively consistent with analytical predictions for cylindrical ferromagnetic NTs by Landeros *et al.* [11].

If we consider NTs having end vortices of opposing circulation sense, a similar phase boundary can be defined between a mixed state configuration with opposing end vortices and an opposing vortex state incorporating a Néel wall [26]. The transition from an axial central domain, found in the mixed state, to the Néel domain wall can be quantified by the presence of inflection points in plots of  $M_n/|M|$  along  $\hat{n}$ . Unfortunately, the available spatial resolution of XMCD-PEEM is not sufficient to clearly determine the inflection points and therefore to distinguish between these two states.

To test the robustness of the remnant magnetization configurations, for some NTs, we take a second set of XMCD-PEEM images in remnance after applying 40 mT along  $\hat{n}$  to saturate the NTs *in situ*. In eleven cases, the measured remnant configuration is observed to be identical to the one initially measured, while in six cases the relative circulation sense of the end vortices changes. According to the simulations, in these six cases, the dimensions of the NTs are such that a matching or opposing circulation sense does not significantly affect its magnetic energy [26]. These include long NTs in mixed states and NTs calculated to be close to the phase boundary between where equal circulation sense begins to be favored. Sample imperfections may trigger the change in relative circulation sense in such NTs.

## V. CONCLUSION

We use XMCD-PEEM to image the remnant magnetization configuration of CoFeB and Py NTs of a variety of lengths. Our study reveals that short NTs can occupy a stable global vortex state in remanence. Consistent with an analytical theory by Landeros *et al.* [11] and our own numerical simulations, the NT length-to-diameter ratio is found to play a crucial role in stabilizing the global vortex state. XMCD-PEEM images of the equilibrium magnetization configurations show that the relative circulation sense of vortex ends in real NTs is less controlled than expected from simulations. As a result, short NTs are found not only in remnant global vortex states, but also in opposing vortex states, which include a Néel wall between two opposing vortices. Additional simulations suggest that sample imperfections including variations in thickness and deviations from a perfect geometry are responsible for this discrepancy. Still, our magnetic images of global vortex states show that the most important properties predicted for idealized ferromagnetic NTs have been realized in real structures. They also demonstrate the programming of the equilibrium magnetic configuration of a ferromagnetic NT via geometry, a result consistent with long-standing theoretical predictions.

## ACKNOWLEDGMENTS

The authors thank Jaianth Vijayakumar, David Bracher, and Patrick Appel for technical support. Part of this work was performed at the Surface/Interface: Microscopy (SIM) beamline of the Swiss Light Source, Paul Scherrer Institut, Villigen, Switzerland. We acknowledge the support of the Canton Aargau, the Swiss Nanoscience Institute, the Swiss National Science Foundation (SNSF) under Grant No. 200020-159893, the NCCR Quantum Science and Technology (QSIT), and Deutsche Forschungsgemeinschaft in the Schwerpunkt Programm “Spin-caloric transport phenomena” SPP1538 via Project No. GR1640/5-2. While in the review process with this manuscript, we learned of new XMCD-PEEM imaging experiments showing vortex-like multidomains in CoNiB NTs [37].

## APPENDIX A: SAMPLE PREPARATION

Ferromagnetic NTs are made by depositing a thin magnetic film on template GaAs NWs. These templates are grown by

molecular beam epitaxy on a Si (111) substrate using Ga droplets as catalysts [28]. For the CoFeB NTs, CoFeB is then magnetron-sputtered on the NWs, producing an amorphous and homogeneous 30-nm-thick shell [31]. For the Py NTs, a 30-nm-thick polycrystalline shell of  $\text{Ni}_{80}\text{Fe}_{20}$  is deposited by thermal evaporation [32]. During both depositions, the wafers of upright and well-separated GaAs NWs are mounted with a  $35^\circ$  angle between the long axis of the NWs and the deposition direction. The wafers are then continuously rotated to achieve a conformal coating.

## APPENDIX B: XMCD-PEEM CONTRAST

$I_\sigma^\pm$  at any location is proportional to both on the intensity of the incident  $\sigma^\pm$  x rays and their absorption at that location. Absorption of  $\sigma^\pm$  x rays is proportional to the projection of the magnetic moment along  $\hat{k}$ . Therefore, positive (red) or negative (blue)  $I_{\text{XMCD}}$  represents near surface magnetization either parallel or antiparallel with  $\hat{k}$ , respectively. For photoemission excited by x rays that have previously passed through magnetic material, however, the absorption in the traversed volume must also be considered [7,8,25]. In our images, such magnetic contrast appears in the x-ray shadow of the NT on the non-magnetic substrate. Since the absorption of  $\sigma^\pm$  x rays is proportional to the projection of the magnetic moment along  $\hat{k}$ , there is also a proportional attenuation of  $\sigma^\pm$  x rays transmitted through the NT and incident in the shadow. The resulting  $I_\sigma^\pm$  is therefore proportional to the magnetization of the volume traversed by the x rays. This proportionality has opposite sign compared to that at a magnetic surface, i.e., positive (red) or negative (blue)  $I_{\text{XMCD}}$  results from volume magnetization either antiparallel or parallel to  $\hat{k}$ , respectively. Combining these two types of contrast, we extract information about both the surface and volume magnetization of the measured NTs [25]. The roughly 100-nm spatial resolution of the XMCD-PEEM images depends on the quality of the focus and properties of the sample, including morphology and cleanliness.

The shape and position of the outlines of the NTs, shown in the figures as dashed lines, are determined by overlaying SEM, PEEM, and XMCD-PEEM images. First outlines of the NTs and of the Au alignment markers are taken from SEM images. Adjusting for the known magnifications, these outlines are aligned on top of the PEEM image of the same area. PEEM contrast is brightest on metallic surfaces, allowing accurate alignment of the outlines taken from the SEMs with PEEM features due to both the surface of the NTs and the alignment markers. By switching to XMCD-PEEM contrast of the same area, we preserve the alignment and obtain outlines of the NTs overlaid onto the corresponding XMCD-PEEM image.

## APPENDIX C: MUMAX3 SIMULATIONS

We set  $\mu_0 M_S$  to its measured value of 1.3 T and 0.8 T and the exchange stiffness to  $A_{\text{ex}} = 28$  pJ/m and 13 pJ/m for CoFeB and Py, respectively. No magneto-crystalline or growth-induced anisotropies are included in our model. In the simulations, space is discretized to 5 nm and thermal fluctuations are not included.

To rule out spurious effects due to the discretization of the numerical cells, we ensure that our results are robust down to a cell size of 1 nm, which is much smaller than the dipolar exchange length  $\Delta_d = \sqrt{2A_{\text{ex}}/\mu_0 M_S^2} \simeq 10$  nm. For cell sizes 1 nm or larger, we find numerical artifacts in the calculations of the energy difference between configurations showing vortices with matching or opposing circulation sense. In particular, insufficient discretization leads to a spurious region in the parameter space, where the opposing vortex configuration is the lowest energy state. As the cell-size is reduced from 10 nm down to 1 nm, this region disappears. It becomes clear that, in fact, there is no region in the diameter versus length phase diagram where the opposing configuration is the lowest energy state. For short tubes, the matching vortex configuration (global vortex state) is the lowest energy state; for long tubes, both matching and opposing vortex configurations have the same energy [26].

- 
- [1] R. P. Cowburn and M. E. Welland, *Science* **287**, 1466 (2000).
  - [2] M. M. Maqableh, X. Huang, S.-Y. Sung, K. S. M. Reddy, G. Norby, R. H. Victora, and B. J. H. Stadler, *Nano Lett.* **12**, 4102 (2012).
  - [3] S. Khizroev, M. H. Kryder, D. Litvinov, and D. A. Thompson, *Appl. Phys. Lett.* **81**, 2256 (2002).
  - [4] M. Poggio and C. L. Degen, *Nanotechnology* **21**, 342001 (2010).
  - [5] H. Campanella, M. Jaafar, J. Llobet, J. Esteve, M. Vázquez, A. Asenjo, R. P. d. Real, and J. A. Plaza, *Nanotechnology* **22**, 505301 (2011).
  - [6] X. F. Han, Z. C. Wen, and H. X. Wei, *J. Appl. Phys.* **103**, 07E933 (2008).
  - [7] S. Jamet, S. Da Col, N. Rougemaille, A. Wartelle, A. Locatelli, T. O. Mentes, B. Santos Burgos, R. Afid, L. Cagnon, S. Bochmann, J. Bachmann, O. Fruchart, and J. C. Toussaint, *Phys. Rev. B* **92**, 144428 (2015).
  - [8] S. Da Col, S. Jamet, N. Rougemaille, A. Locatelli, T. O. Mentes, B. S. Burgos, R. Afid, M. Darques, L. Cagnon, J. C. Toussaint, and O. Fruchart, *Phys. Rev. B* **89**, 180405 (2014).
  - [9] N. A. Usov, A. Zhukov, and J. Gonzalez, *J. Magn. Magn. Mater.* **316**, 255 (2007).
  - [10] P. Landeros, S. Allende, J. Escrig, E. Salcedo, D. Altbir, and E. E. Vogel, *Appl. Phys. Lett.* **90**, 102501 (2007).
  - [11] P. Landeros, O. J. Suarez, A. Cuchillo, and P. Vargas, *Phys. Rev. B* **79**, 024404 (2009).
  - [12] Y. Gaididei, V. P. Kravchuk, and D. D. Sheka, *Phys. Rev. Lett.* **112**, 257203 (2014).
  - [13] R. Streubel, P. Fischer, F. Kronast, V. P. Kravchuk, D. D. Sheka, Yuri Gaididei, O. G. Schmidt, and D. Makarov, *J. Phys. D: Appl. Phys.* **49**, 363001 (2016).
  - [14] J. A. Otálora, M. Yan, H. Schultheiss, R. Hertel, and A. Kákay, *Phys. Rev. Lett.* **117**, 227203 (2016).
  - [15] M. Yan, A. Kákay, C. Andreas, and R. Hertel, *Phys. Rev. B* **88**, 220412 (2013).

- [16] A.-P. Chen, J. M. Gonzalez, and K. Y. Guslienko, *J. Appl. Phys.* **109**, 073923 (2011).
- [17] A. P. Chen, N. A. Usov, J. M. Blanco, and J. Gonzalez, *J. Magn. Mater.* **316**, e317 (2007).
- [18] A. P. Chen, K. Y. Guslienko, and J. Gonzalez, *J. Appl. Phys.* **108**, 083920 (2010).
- [19] D. Li, R. S. Thompson, G. Bergmann, and J. G. Lu, *Adv. Mater.* **20**, 4575 (2008).
- [20] D. Ruffer, R. Huber, P. Berberich, S. Albert, E. Russo-Averchi, M. Heiss, J. Arbiol, A. F. i. Morral, and D. Grundler, *Nanoscale* **4**, 4989 (2012).
- [21] D. P. Weber, D. Ruffer, A. Buchter, F. Xue, E. Russo-Averchi, R. Huber, P. Berberich, J. Arbiol, A. Fontcuberta i Morral, D. Grundler, and M. Poggio, *Nano Lett.* **12**, 6139 (2012).
- [22] R. Streubel, J. Lee, D. Makarov, M.-Y. Im, D. Karnaushenko, L. Han, R. Schäfer, P. Fischer, S.-K. Kim, and O. G. Schmidt, *Adv. Mater.* **26**, 316 (2014).
- [23] R. Streubel, L. Han, F. Kronast, A. A. Ünal, O. G. Schmidt, and D. Makarov, *Nano Lett.* **14**, 3981 (2014).
- [24] R. Streubel, F. Kronast, P. Fischer, D. Parkinson, O. G. Schmidt, and D. Makarov, *Nat. Commun.* **6**, 7612 (2015).
- [25] J. Kimling, F. Kronast, S. Martens, T. Böhnert, M. Martens, J. Herrero-Albillos, L. Tati-Bismaths, U. Merkt, K. Nielsch, and G. Meier, *Phys. Rev. B* **84**, 174406 (2011).
- [26] See Supplemental Material at <http://link.aps.org/supplemental/10.1103/PhysRevB.96.024423> for XMCD-PEEM and SEM images of all measured NTs, phase diagrams of the relative sense of vortex circulation, phase diagrams showing the transition between mixed and opposing vortex states, and plots of vortex length as a function of NT diameter.
- [27] A. T. Hindmarch, C. J. Kinane, M. MacKenzie, J. N. Chapman, M. Henini, D. Taylor, D. A. Arena, J. Dvorak, B. J. Hickey, and C. H. Marrows, *Phys. Rev. Lett.* **100**, 117201 (2008).
- [28] D. Ruffer, M. Slot, R. Huber, T. Schwarze, F. Heimbach, G. Tütüncüoglu, F. Matteini, E. Russo-Averchi, A. Kovács, R. Dunin-Borkowski, R. R. Zamani, J. R. Morante, J. Arbiol, A. F. i. Morral, and D. Grundler, *APL Mater.* **2**, 076112 (2014).
- [29] T. Schwarze and D. Grundler, *Appl. Phys. Lett.* **102**, 222412 (2013).
- [30] K. Baumgaertl, F. Heimbach, S. Maendl, D. Ruffer, A. Fontcuberta i Morral, and D. Grundler, *Appl. Phys. Lett.* **108**, 132408 (2016).
- [31] B. Gross, D. P. Weber, D. Ruffer, A. Buchter, F. Heimbach, A. Fontcuberta i Morral, D. Grundler, and M. Poggio, *Phys. Rev. B* **93**, 064409 (2016).
- [32] A. Buchter, R. Wölbing, M. Wyss, O. F. Kieler, T. Weimann, J. Kohlmann, A. B. Zorin, D. Ruffer, F. Matteini, G. Tütüncüoglu, F. Heimbach, A. Kleibert, A. Fontcuberta i Morral, D. Grundler, R. Kleiner, D. Koelle, and M. Poggio, *Phys. Rev. B* **92**, 214432 (2015).
- [33] L. L. Guyader, A. Kleibert, A. F. Rodríguez, S. E. Moussaoui, A. Balan, M. Buzzi, J. Raabe, and F. Nolting, *J. Electron Spectrosc. Relat. Phenom.* **185**, 371 (2012).
- [34] A. Vansteenkiste, J. Leliaert, M. Dvornik, M. Helsen, F. Garcia-Sanchez, and B. Van Waeyenberge, *AIP Adv.* **4**, 107133 (2014).
- [35] Z. Wang, K. Reimann, M. Woerner, T. Elsaesser, D. Hofstetter, J. Hwang, W. J. Schaff, and L. F. Eastman, *Phys. Rev. Lett.* **94**, 137208 (2005).
- [36] J. Lee, D. Suess, T. Schrefl, K. H. Oh, and J. Fidler, *J. Magn. Mater.* **310**, 2445 (2007).
- [37] M. Staño, S. Schaefer, A. Wartelle, M. Rioult, R. Belkhou, A. Sala, T. O. Menteş, A. Locatelli, L. Cagnon, B. Trapp, S. Bochmann, S. Martin, E. Gautier, J.-C. Toussaint, W. Ensinger, and O. Fruchart, [arXiv:1704.06614](https://arxiv.org/abs/1704.06614).